NANO LETTERS

pubs.acs.org/NanoLett Letter

An All-Dielectric Polaritonic Metasurface with a Giant Nonlinear Optical Response

Raktim Sarma,* Jiaming Xu, Domenico de Ceglia, Luca Carletti, Salvatore Campione, John Klem, Michael B. Sinclair, Mikhail A. Belkin, and Igal Brener*

Cite This: *Nano Lett.* 2022, 22, 896−903 Read Online

ACCESS | Metrics & More | Article Recommendations | Supporting Information

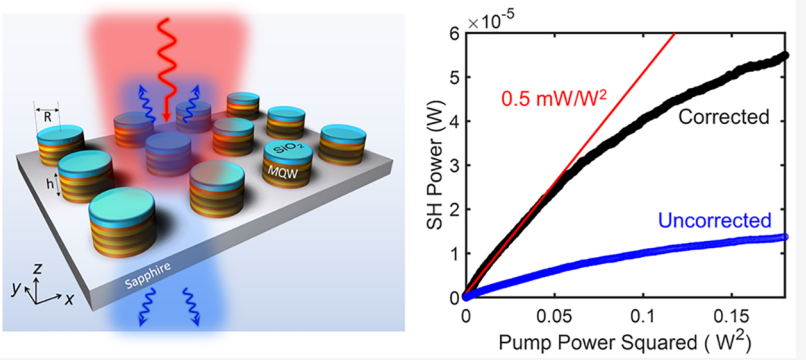

ABSTRACT: Enhancing the efficiency of second-harmonic generation using all-dielectric metasurfaces to date has mostly focused on electromagnetic engineering of optical modes in the meta-atom. Further advances in nonlinear conversion efficiencies can be gained by engineering the material nonlinearities at the nanoscale, however this cannot be achieved using conventional materials. Semiconductor heterostructures that support resonant nonlinearities using quantum engineered intersubband transitions can provide this new degree of freedom. By simultaneously optimizing the heterostructures and meta-atoms, we experimentally realize an all-dielectric polaritonic metasurface with a maximum second-harmonic generation power conversion factor of 0.5 mW/W^2 and power conversion efficiencies of 0.015% at nominal pump intensities of 11 kW/cm^2. These conversion efficiencies are higher than the record values reported to date in all-dielectric nonlinear metasurfaces but with 3 orders of magnitude lower pump power. Our results therefore open a new direction for designing efficient nonlinear all-dielectric metasurfaces for new classical and quantum light sources.

KEYWORDS: *Nonlinear metasurfaces, All-Dielectric metasurfaces, Strong light-matter interaction, Second-harmonic generation, Polaritons, III−V semiconductors, Intersubband transitions*

Nonlinear optics, which is one of most prominent areas of research in photonics, has for a long time relied on high power lasers and bulk nonlinear crystals to realize efficient nonlinear optical phenomena such as second-harmonic generation (SHG). Bulk crystals, albeit efficient, are subject to phase matching requirements which limit their applicability.[1] All-dielectric metasurfaces have recently led to a paradigm shift in nonlinear optics, as these nanostructures, because of their subwavelength thickness, low loss, high damage thresholds, and resonant field enhancements, allow for efficient SHG without the requirement of phase matching.[2,3] The absence of phase matching constraints allows metasurfaces to operate without any stringent angular alignment requirements with respect to the incident beam. In addition, the field enhancements induced by the resonant modes of the metasurface at the pump and harmonic frequencies allow for efficient nonlinear wave mixing.[4−9] Furthermore, the metasurfaces can also be designed to control the wavefront of the nonlinear beams.[10−13]

To date, the optimization strategies of SHG efficiency in all-dielectric metasurfaces have mostly concentrated on (1) increasing quality (Q) factors of the resonant modes at the pump frequency to increase the field enhancement,[14−17] (2) stacking multiple metasurface layers on top of one another,[18] or (3) optimizing the nonlinear overlap factor of the fundamental and SH modes in the meta-atoms.[19] Among these three approaches, the maximum efficiency has been

Received: August 27, 2021
Revised: January 7, 2022
Published: January 19, 2022

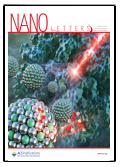

https://doi.org/10.1021/acs.nanolett.1c03325
Nano Lett. 2022, 22, 896−903

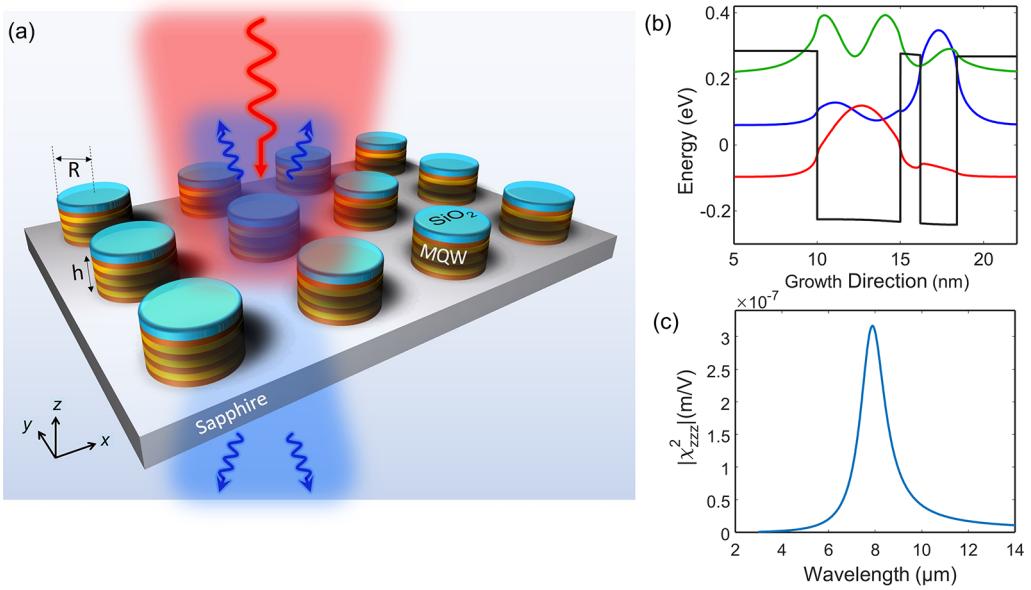

Figure 1. Working principle and optimization of the matter component of the all-dielectric polaritonic nonlinear metasurface. (a) Schematic of the nonlinear metasurface. The height (h) of all the fabricated cylindrical Mie resonators is 1.5 μm. The radii (R) of the cylinders are varied to vary the spectral position of the Mie photonic resonances in order to couple incident pump light to the fundamental intersubband transition at 7.8 μm. (b) The 8-band k.p band structure calculation of the conduction band of a single period of the multi-QW heterostructure used in this study. The thicknesses of the two asymmetric coupled quantum wells are optimized to support three equally spaced energy levels separated by 156 meV (7.8 μm) such that it can generate SH signal at 312 meV (3.9 μm). The layer structure of a single period of the heterostructure is given as **10 nm**/5 nm/**1.2 nm**/2.2 nm/**10 nm**, where $Al_{0.52}In_{0.48}As$ barriers are shown in bold and $In_{0.53}Ga_{0.47}As$ wells are shown in a regular font. All $In_{0.53}Ga_{0.47}As$ layers are n-doped with doping density of 2×10^{18} cm^{-3} (c) Calculated value of the intersubband nonlinear susceptibility of the multi-QW structure shown in (b) as a function of the pump wavelength.

observed for the first approach where resonant modes with ultrahigh Q factor at the pump frequency are used for SHG. For example, electromagnetically engineered quasi-bound-state-in-the-continuum (BIC) modes with ultrahigh Q factors excited via appropriately designed polarized pump beams have been used to demonstrate ultrahigh SHG power conversion efficiencies of ~0.004%.[14−17]

Another degree of freedom, which has been unexplored in the context of nonlinear all-dielectric metasurfaces, is engineering the magnitude of the nonlinear susceptibility of the medium that constitutes the meta-atoms. Bulk semiconductors with large nonlinear coefficients, such as GaAs/AlGaAs (d_{14} ~ 200 pm/V[5,8]), have been used for designing metasurfaces for SHG, however microscopic control of the magnitude of the nonlinearity of such semiconductors is not straightforward. Additionally, there have been efforts to control the directivity of the generated second-harmonic to enhance the SH collection efficiency. This has been explored by tailoring the geometries of the meta-atoms,[20−22] the polarization and incidence angle of the pump beam,[23,24] and the crystal orientations of the semiconductors.[25,26] While these efforts indeed increased collection efficiency, however, the total SHG efficiency was not shown to be significantly enhanced by these efforts which ultimately depends on the magnitude of the material nonlinear susceptibility. Since the efficiency of SHG scales as the square of the nonlinear susceptibility ($\chi^{(2)}$), the ability to engineer the magnitude of the $\chi^{(2)}$ tensor elements in all-dielectric metasurfaces is of paramount importance for optimizing SHG efficiency and is on equal footing with electromagnetic mode engineering. Furthermore, an approach involving only increasing the Q factor may have limitations since at relatively high pump powers metasurfaces with ultrahigh Q factors may suffer from impairments such as nonlinear two-photon absorption and free-carrier absorption generated by two-photon absorption.[27]

In this work, we demonstrate the possibility of enhancing the SHG efficiency of all-dielectric metasurfaces by engineering the nonlinearity of the dielectric medium that constitutes the meta-atoms. Using intersubband transitions (ISTs) in multi-quantum-wells (multi-QW) it is possible to engineer one of the largest magnitudes of $\chi^{(2)}$ available in condensed matter systems.[28] This has been exploited in light-matter coupled plasmonic metasurfaces and meta-grating structures to achieve ultrahigh SHG conversion efficiencies.[10,29−31] Here, we demonstrate that by embedding multi-QW semiconductor heterostructures that support ISTs within all-dielectric resonators that support Mie type modes, it is possible to polaritonically couple ISTs to Mie modes and achieve a SHG conversion factor of 0.5 mW/W^2 which is much larger than the record-high SHG conversion factors demonstrated so far using all-dielectric metasurfaces based on nonresonant nonlinearities.[14−17] Furthermore, these metasurfaces can operate at normal and off-normal incidence; unlike BIC nonlinear metasurfaces,[16,17] they do not require any special polarization of the pump beam.

In addition to giant nonlinearities, IST-based Mie metasurfaces have additional advantages over their plasmonic or dielectric based counterparts. For example, the $\chi^{(2)}$ due to ISTs in the multi-QWs is proportional to the product of three dipole moments, the signs of which can be flipped by reversing the sequence of the growth of the heterostructure. This implies that by designing the growth sequence, it is possible to grow a heterostructure which can have an arbitrary magnitude and sign of $\chi^{(2)}$ along the growth direction.[32] Such microscopic

https://doi.org/10.1021/acs.nanolett.1c03325
Nano Lett. 2022, 22, 896−903

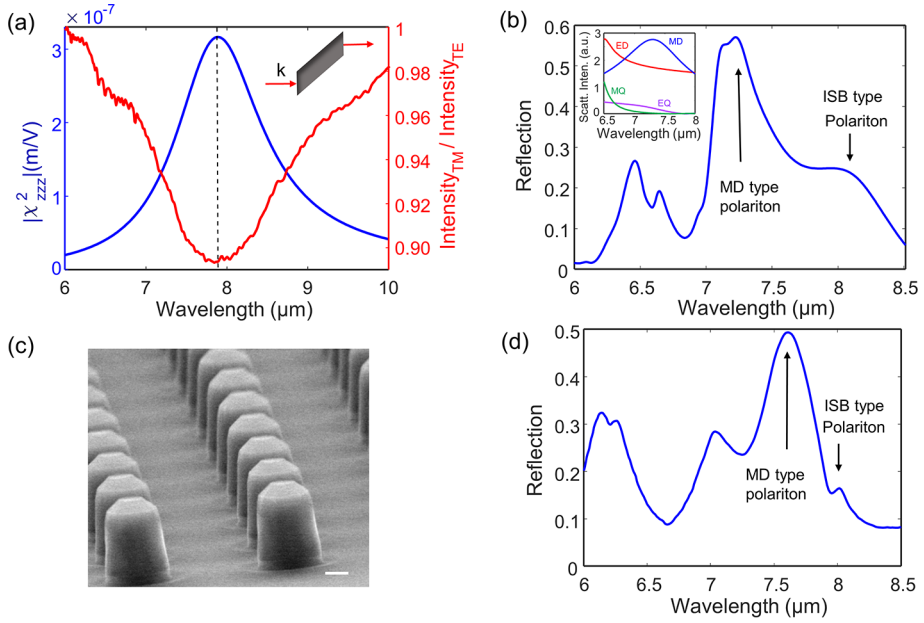

Figure 2. Optimization of the photonic component of the all-dielectric polaritonic nonlinear metasurface. (a) Numerically calculated value of the intersubband nonlinear susceptibility of the multi-QW structure (blue line and left vertical axis) as a function of the pump wavelength overlaid with experimentally measured intersubband normalized transmission spectrum (red line and right vertical axis) of the multi-QW heterostructures used in this study. The inset shows the waveguide configuration used for the normalized transmission measurements with the input direction (k) indicated. The spectrum is produced by taking the ratio of the intensity of the transmitted transverse magnetic polarized input light to the intensity of the transmitted transverse electric polarized input light. (Further details on the IST transmission measurements are provided in the Supporting Information.) The dip in the normalized transmission spectrum corresponds to the peak of absorption induced by the IST at ∼7.8 μm. (b) Finite-difference-time domain simulation results of reflectance from a metasurface with cylinders of R = 1.4 μm. The simulation includes the effect of ISTs in the real and imaginary parts of the dielectric constant of the multi-QW layer. The resonators are optimized to support a magnetic dipole (MD) mode slightly spectrally detuned from the IST. Formation of intersubband polaritons can be seen due to coupling of the MD mode to the IST. The inset shows the simulated multipolar decomposition of the scattering-cross section intensity (scatt. inten.) in arbitrary units (a.u.) of an infinite array of cylinders of R = 1.4 μm without the presence of ISTs. MD, ED, MQ, EQ are magnetic dipole, electric dipole, magnetic quadrupole, electric quadrupole, respectively. The scattering cross section shows a peak for MD near the IST wavelength confirming that the bare cavity supports an MD mode (c) Side view scanning electron micrograph of one of the fabricated metasurfaces with cylinders of R = 1.4 μm. The white scale bar corresponds to 1 μm. (d) Experimentally measured linear reflectance spectra of a metasurface with cylinders of R = 1.4 μm. Rabi splitting of the MD resonance can be seen indicating strong light−matter coupling between the MD resonance and the IST. The experimental results agree well with the simulations shown in (b).

control of the nonlinearity along the z-axis is extremely difficult to achieve using nonlinearities from bulk conventional semiconductors such as GaAs, AlGaAs, or GaP and can allow for optimizing the nonlinear overlap integrals by tailoring the field overlap of multimode resonances in the z-direction with the optical nonlinearity. Furthermore, since the spatial field profiles and polarization of Mie modes can be controlled using shape, size, and symmetry of the resonators, all-dielectric Mie-metasurfaces will offer more flexibility in exploiting such mode overlap techniques as compared to plasmonic meta-surfaces[4,10,29,30] or all-dielectric meta-grating-based structures[31] whose fields are evanescent and exponentially decaying away from the sample surface. Finally, since Mie modes are volume modes, that is, the electromagnetic fields are confined within the meta-atom (as opposed to plasmonic metasurfaces[4,10,29,30] or leaky mode resonances[31] where fields are evanescent), the light−matter interaction volumes in IST-based Mie metasurfaces can be easily engineered and increased by appropriate design of the shape or size of the meta-atom and heterostructure embedded within it.

The nonlinear all-dielectric metasurfaces used in this study consist of arrays of periodically spaced cylindrical dielectric resonators fabricated from III−V semiconductor heterostructures with n-doped $In_{0.53}Ga_{0.47}As/Al_{0.52}In_{0.48}As$ multi-QWs (Figure 1a). The resonant wavelengths of the Mie modes depend on the geometric parameters of the cylinders and the array and can be spectrally tuned by controlling the radius (R), height (h), and periodicity (p); h was fixed at 1.5 μm and R was varied to spectrally scale the Mie resonances. The periodicity was fixed at $3R$ to limit near-field coupling effects between neighboring meta-atoms and to avoid significant alteration of the magnetic-resonance feature in the linear spectrum. The details of the multi-QW structure and fabrication methods are given in the Supporting Information.

The "matter" component of our polaritonic nonlinear metasurface consists of ISTs supported by the multi-QWs and the "light" component consists of the Mie photonic modes supported by the cylindrical resonators. While the matter component determines the magnitude of $\chi^{(2)}$, the field enhancements and coupling efficiency of the incident pump light to the ISTs are determined by the photonic component. To maximize the magnitude of $\chi^{(2)}$, we optimized the multi-QW heterostructure to support three equally spaced electronic energy levels with energy separation of approximately 156 meV (7.8 μm). Such an asymmetric QW design allows us to have optical transitions at both the fundamental pump wavelength (7.8 μm) and SH wavelength (3.9 μm) and thereby create a quantum system with a doubly resonant $\chi^{(2)}$.[28] Because of the

https://doi.org/10.1021/acs.nanolett.1c03325
Nano Lett. 2022, 22, 896−903

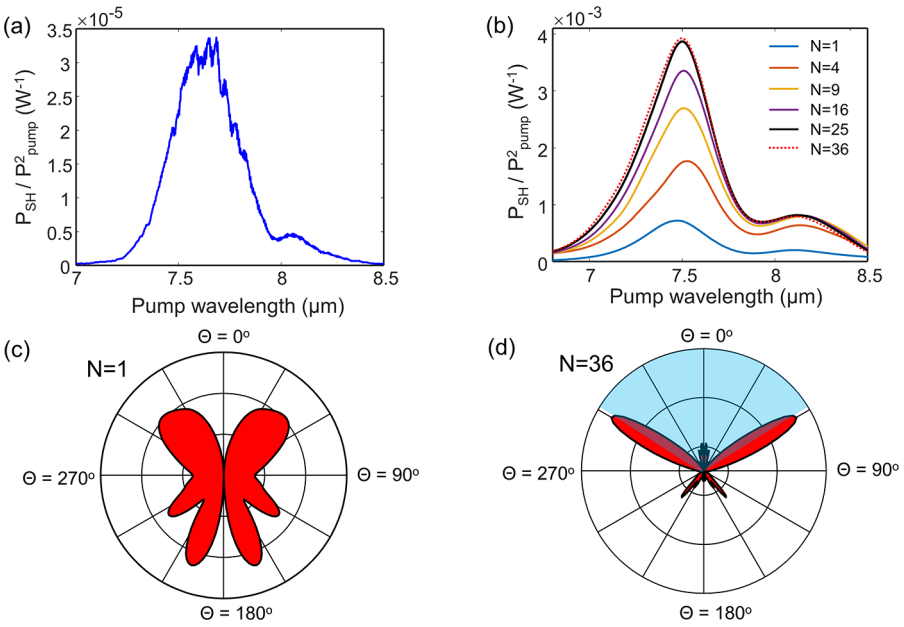

Figure 3. Experimental measurements and numerical simulation of SHG from metasurfaces with MD resonances coupled to ISTs. (a) Experimentally measured reflected SH power conversion efficiency in normalized units for normal incidence as a function of pump wavelength from a metasurface with cylinders of R = 1.4 μm. Two peaks at ∼7.6 μm and ∼8 μm are observed corresponding to the two polariton branches. The maximum SHG efficiency is observed at a pump wavelength of ∼7.65 μm. (b) Numerically calculated reflected SH power conversion efficiency in normalized units for normal incidence as a function of pump wavelength from metasurfaces with cylinders of R = 1.4 μm. The simulated metasurfaces are finite arrays consisting of different number of meta-atoms (N). N = 1 corresponds to a single isolated meta-atom, whereas for N > 1, the meta-atoms are arranged in a $\sqrt{N} \times \sqrt{N}$ array with period = 3R. The spectral dependence of SHG efficiencies is similar for all cases and agrees well with experimental results shown in (a). The magnitude of the SHG efficiency first increases rapidly for N < 25 and then converges for N > 25. (c,d) Calculated far-field emission pattern of SH as a function of angle (θ) in the x−z plane from a single cylindrical resonator (N = 1) with R = 1.4 μm (c) and from a 6 × 6 (d) array (N = 36) at a pump wavelength of 7.65 μm with pump intensity of 10 kW/cm^2. For N = 36, the reflected SH lobes become narrower and emit at angles closer to the first diffraction order. The shaded cone shows the solid angle corresponding to the numerical aperture of the collection optics.

IST selection rules, only out-of-plane polarized electric fields can couple to the ISTs and therefore the only nonzero element of the $\chi^{(2)}$-tensor in such a system is $\chi^{(2)}_{zzz}$. Figure 1b shows an 8-band k.p band structure calculation of the conduction band of a single period of the multi-QW system used in this study, and the corresponding calculated $\chi^{(2)}_{zzz}$ is shown in Figure 1c (calculation details in Supporting Information).

Next, we engineered the light or photonic component, that is, the Mie modes of the cylindrical resonators, to satisfy two conditions: (1) efficient coupling of the incident pump light to the ISTs; and (2) maximize the product of $|\chi^{(2)}|$ and field enhancement, f_p, ($f_p = |E_z/E_{inc}|$ where E_{inc} is the amplitude of the electric field in the incident wave) of the E_z field component at the pump wavelength as the SHG efficiency is proportional to $|\chi^{(2)}_{zzz} f_p^2|^2$. To simultaneously satisfy both conditions, the first metasurface we designed had meta-atoms that supported the lowest order magnetic dipole (MD) mode at a wavelength slightly detuned from the fundamental IST wavelength (7.8 μm) but still within the linewidth of the IST resonance. The IST resonance linewidth can be inferred from the experimentally measured normalized transmission spectrum of the multi-QW stack shown in Figure 2a. Since the MD mode has strong z-directed electric field components (due to its circulating out-of-plane electric fields), choosing the MD mode allows us to strongly couple normally incident pump light to the ISTs. In addition, slight detuning of the MD mode with respect to the IST resonance is necessary to maximize $|\chi^{(2)}_{zzz} f_p^2|^2$ because, unlike virtual transitions in bulk crystals, real electronic transitions associated with ISTs are accompanied by absorption losses. In fact, as shown in Figure 2a, the maximum of $|\chi^{(2)}|$ and IST-induced absorption spectrally overlap.

Since the ISTs affect the linear optical response and field enhancements of the metasurface, to optimize the photonic component, we simulated the entire light-matter coupled system (calculation details in Supporting Information). Figure 2b shows the calculated linear reflectance spectrum of one of the optimized resonators (R = 1.4 μm) used in this study and the corresponding field enhancements of the out-of-plane ($|E_z|$) field components are shown in the Supporting Information (Figure S1a). As shown in Figure 2b, the optimized meta-atoms show a polaritonic linear response where two polariton branches corresponding to an "MD photonic mode type" (∼7.3 μm) and an "IST matter type" (∼8 μm) can be seen. The formation of intersubband polaritons confirms efficient coupling of the incident pump light to the ISTs.

After optimizing both the matter and photonic components, we fabricated the nonlinear metasurface using electron beam lithography and etching techniques (fabrication details in Supporting Information). Figure 2c shows a side view scanning electron micrograph of the fabricated metasurface and the corresponding experimentally measured linear reflectance spectrum obtained using a Fourier-transform infrared spectroscopy (FTIR) microscope is shown in Figure 2d. Overall, a good qualitative agreement between experiment (Figure 2d) and simulations (Figure 2b) can be seen with slight spectral shifting of the resonances, which we attribute to a slight mismatch of geometrical parameters of fabricated samples

https://doi.org/10.1021/acs.nanolett.1c03325
Nano Lett. 2022, 22, 896−903

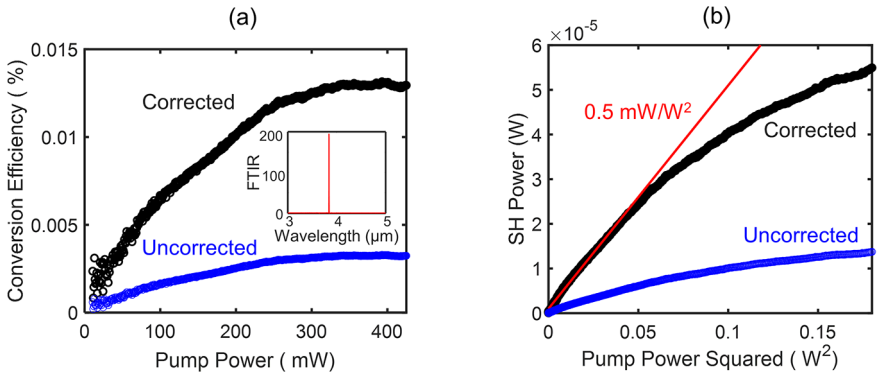

Figure 4. Experimental measurements of SHG at a single pump wavelength from metasurfaces with MD resonances coupled to ISTs. (a) Experimentally measured SH power conversion efficiency (defined as the ratio of SH power to pump power) as a function of incident peak pump power at a pump wavelength of 7.65 μm of the metasurface with R = 1.4 μm. The figure includes the raw data (uncorrected) as well as the data corrected for the limited collection efficiency at SH wavelength. The inset shows the corresponding experimentally measured FTIR spectrum of SH radiation. Only one spectral peak corresponding to half the pump wavelength can be seen confirming SHG process. (b) Experimentally measured peak SH power as a function of square of incident peak pump power for the same metasurface and pump wavelength as in (a). The figure includes the raw data (uncorrected) as well as the data corrected for the limited collection efficiency at 7.65 μm. The slope of the linear fit (red line) at lower pump powers determines the nonlinear conversion factor η which is equal to 0.5 mW/W^2. The deviation of the slope at higher pump powers is seen due to the saturation effect of the ISTs.

compared to numerical simulations. As expected, clear splitting of the MD resonance at ~7.8 μm can be observed due to formation of intersubband polaritons which is a signature of strong light−matter coupling.[33]

Next, we experimentally measured the generated SH spectra in a reflection geometry from the metasurface shown in Figure 2c (details of experimental setup and nonlinear measurements are in Supporting Information). Figure 3a shows the experimental results for normalized SHG efficiency. Peaks can be seen at ~7.6 μm and ~8 μm which correspond to the two polariton branches. Furthermore, because of larger field enhancements at wavelengths slightly shorter than the IST wavelength of 7.8 μm (Figure S1a in Supporting Information), the SHG efficiency is also correspondingly larger at those wavelengths and the maximum is observed at a pump wavelength of λ_p = 7.65 μm.

To better understand and correctly quantify the magnitude of SHG efficiency of our experimental sample, we performed nonlinear numerical simulations using a frequency domain, finite-element method (COMSOL) (details in Supporting Information). Since the measured SHG efficiency depends on both the SH generation efficiency of the metasurface as well as the collection efficiency of the experimental setup, we investigated both of these factors. In our experiment, the metasurface has a finite number of meta-atoms and is illuminated with a finite spot size of radius ~22 μm. Therefore, accurate predictions of the SH generation efficiencies require simulation of finite sized arrays of resonators. Figure 3b shows the numerically calculated SH efficiency for finite arrays of different sizes. We observe that the spectral dependence of normalized SHG efficiencies is similar for different array sizes and matches the experimental data very well. In addition, the absolute magnitude of the SHG efficiency rapidly increases as the size of the array increases (for 1 < N < 25, where N is the total number of meta-atoms) and then converges (N > 25) to a value ~4 mW/W^2. This trend is associated with the small near-field coupling between neighboring meta-atoms, which leads to an initial increase of the field enhancement at the pump wavelength with increasing size of the array (Figure S1a,b in Supporting Information). The maximum value of the field enhancement saturates beyond a certain array size.

Another aspect that limits the magnitude of the experimentally measured SHG efficiency is the limited collection efficiency due to the finite numerical aperture (NA) of the optics collecting the SH signal. Figure 3c shows the calculated SH far field emission pattern in the x−z plane of a single meta-atom with R = 1.4 μm pumped at 7.65 μm. The meta-atom radiates SH power in both reflection and transmission directions. Because of the in-plane inversion symmetry of the cylindrical resonator structures along with the presence of only a single element $\chi^{(2)}_{zzz}$ in the second-order nonlinear susceptibility tensor, the nonlinear polarization at the SH frequency is induced only in the z-direction. This situation results in the SH being radiated at off-normal angles with zero SH power radiated along the normal direction. For a finite array, because of the periodicity and array factor, the lobes of the SH signal become narrower than the isolated meta-atom and SH fields are diffracted primarily to the first diffraction orders at an angle approximately given by $\sin(\theta_{SH}) = \frac{\lambda_p}{2p}$ which in this case is $\theta_{SH} \sim 65°$ (Figure 3d) Since the numerical aperture of the collection optics used in our experiment is 0.85, only 25% of the emitted SH light (shown by shaded cone in Figure 3d) is collected, and the actual reflected SHG efficiency for the experimental sample is therefore much larger. Furthermore, as shown in Figure 3d, while a single meta-atom radiates SH in both directions (corresponding to reflection and transmission geometries), due to the periodicity of the metasurface, the SHG is primarily diffracted at large angles causing total internal reflection of transmitted SHG in the sapphire substrate. Only a very small amount of SH is transmitted to the far field in the transmission geometry while the majority of the generated SH is trapped in the Sapphire substrate.

The measured reflected SH signal of the metasurface at a fixed pump wavelength λ_p = 7.65 μm as a function of pump power is shown in Figure 4. To correctly estimate the total SH conversion efficiencies of our sample, the measured data was multiplied by a factor of 4 to correct for the limited collection

https://doi.org/10.1021/acs.nanolett.1c03325
Nano Lett. 2022, 22, 896−903

efficiency. The SH power conversion efficiency, defined as the ratio of the SH power to the pump power is shown is Figure 4a. The maximum conversion efficiency is 0.013% at a peak pump intensity of 11 kW/cm^2. The inset in Figure 4a shows the measured spectrum of the SH signal. Only a single narrow spectral peak at one-half of the pump wavelength is seen, which confirms that we indeed observe the SHG process. Finally, to determine the nonlinear conversion factor and to compare to the simulations shown in Figure 3b, we plot in Figure 4b the experimentally measured reflected peak SH power (P_{SH}) as a function of square of peak pump power (P^2_{pump}). The nonlinear SH power conversion factor, $\eta = \frac{P_{SH}}{P^2_{pump}}$, is determined from the slope at lower input powers and is as large as 0.5 mW/W^2. This experimentally measured value is in good agreement with simulations and is within an order of magnitude of the peak value of 4 mW/W^2 predicted by the numerical simulations. To confirm the spectral dependency of the SHG efficiency, we also calculated the effective nonlinear susceptibility of the metasurface (results in Supporting Information). The results (Figure S1c) are in good agreement with the spectral dependence of the computed SHG efficiencies shown in Figure 3b and the experimental SHG measurements shown in Figure 3a.

Finally, we performed experiments to address the problem of low collection efficiency due to diffraction. For maximizing the collection efficiency, we fabricated a metasurface with cylinders of larger radii and coupled the magnetic quadrupole (MQ) mode to the IST at 7.8 μm. The results are given in Supporting Information, and for the MQ resonance, without any correction, we experimentally measured the maximum SH power conversion efficiency to be as large as 0.015% at a peak pump intensity of 11 kW/cm^2 and the normalized conversion factor to be 0.5 mW/W^2 (Figure S3b,c of Supporting Information). We note here that the SH power conversion efficiencies measured in this work are higher than record-high SHG power conversion efficiencies measured using GaAs/AlGaAs or GaP based all-dielectric metasurfaces,[14−17] and we achieved this using 3 orders of magnitude lower pump intensity. The maximum SH power conversion efficiency as well as the normalized power-conversion factor at higher pump intensities presented in this work are also higher compared to what was reported in ref 31 where evanescent fields of leaky-mode-resonances supported by dielectric gratings were used to couple incident pump light to the ISTs. Compared to leaky-mode-resonances,[31] the lower-order Mie modes used in this work have Q factors comparable to the line widths of the ISTs allowing us to better achieve the intricate balance between field enhancements, saturation effects, and magnitude of the nonlinearity which is required to achieve overall higher conversion efficiencies at higher pump intensities.

To conclude, we have presented a proof-of-concept demonstration of an extremely nonlinear all-dielectric polaritonic metasurface, and we envision that the total efficiency of an IST based all-dielectric metasurface can be further optimized (see Supporting Information for details). While we demonstrated SHG in the mid-infrared wavelength range, the IST-based Mie metasurface approach can also be extended to generate SH signal all the way from near- to long-infrared wavelengths using a combination of different material systems[34−36] and quantum-well designs.[37,38] IST-based all-dielectric Mie metasurfaces can therefore offer an exciting and fundamentally new platform for studying nonlinear optics at the nanoscale and can offer new opportunities for developing new classical or quantum light sources[39,40] for various applications ranging from sensing,[41] spectroscopy,[42] active thermography for nondestructive testing,[43] hyperspectral infrared imaging,[44] to optical coherence tomography.[45]

■ ASSOCIATED CONTENT

Supporting Information

The Supporting Information is available free of charge at https://pubs.acs.org/doi/10.1021/acs.nanolett.1c03325.

Linear and nonlinear numerical simulations of finite and infinite arrays of meta-atoms showing field enhancements, SH efficiencies, and effective nonlinear susceptibilities; experimental results of second-harmonic generation using metasurfaces with MQ modes coupled to ISTs; details of experimental and simulation methods; comparison of different approaches for SHG; optimization of SHG using all-dielectric polaritonic intersubband metasurfaces (PDF)

■ AUTHOR INFORMATION

Corresponding Authors

Raktim Sarma − *Sandia National Laboratories, Albuquerque, New Mexico 87123, United States; Center for Integrated Nanotechnologies, Sandia National Laboratories, Albuquerque, New Mexico 87123, United States;* orcid.org/0000-0002-7288-2044; Email: rsarma@sandia.gov

Igal Brener − *Sandia National Laboratories, Albuquerque, New Mexico 87123, United States; Center for Integrated Nanotechnologies, Sandia National Laboratories, Albuquerque, New Mexico 87123, United States;* orcid.org/0000-0002-2139-5182; Email: ibrener@sandia.gov

Authors

Jiaming Xu − *Department of Electrical and Computer Engineering, University of Texas at Austin, Austin, Texas 78712, United States*

Domenico de Ceglia − *Department of Information Engineering, University of Padova, Padua 35122, Italy*

Luca Carletti − *Department of Information Engineering, University of Padova, Padua 35122, Italy; Department of Information Engineering and INO−CNR, University of Brescia, Brescia 25121, Italy;* orcid.org/0000-0001-6268-9817

Salvatore Campione − *Sandia National Laboratories, Albuquerque, New Mexico 87123, United States;* orcid.org/0000-0003-4655-5485

John Klem − *Sandia National Laboratories, Albuquerque, New Mexico 87123, United States*

Michael B. Sinclair − *Sandia National Laboratories, Albuquerque, New Mexico 87123, United States*

Mikhail A. Belkin − *Department of Electrical and Computer Engineering, University of Texas at Austin, Austin, Texas 78712, United States; Walter Schottky Institut, Technische Universitat Munchen, Garching 85748 Bavaria, Germany*

Complete contact information is available at: https://pubs.acs.org/10.1021/acs.nanolett.1c03325

https://doi.org/10.1021/acs.nanolett.1c03325
Nano Lett. 2022, 22, 896−903

Author Contributions

R.S. and J.X. have contributed equally to this work. The manuscript was written through contributions of all authors. All authors have given approval to the final version of the manuscript.

Notes

The authors declare no competing financial interest.

■ ACKNOWLEDGMENTS

This work was supported by the U.S. Department of Energy, Office of Basic Energy Sciences, Division of Materials Sciences and Engineering and performed in part at the Center for Integrated Nanotechnologies, an Office of Science User Facility operated for the U.S. Department of Energy (DOE) Office of Science. Sandia National Laboratories is a multimission laboratory managed and operated by National Technology and Engineering Solutions of Sandia, LLC, a wholly owned subsidiary of Honeywell International, Inc., for the U.S. Department of Energy's National Nuclear Security Administration under contract DE-NA0003525. The University of Texas and the Technical University of Munich members of the team acknowledges financial support from the DARPA NASCENT program. The University of Padova team members were partly supported by MIUR (Italian Minister for Education) under the initiative "Departments of Excellence" (Law 232/2016). This paper describes objective technical results and analysis. Any subjective views or opinions that might be expressed in the paper do not necessarily represent the views of the U.S. Department of Energy or the United States Government.

■ ABBREVIATIONS

SHG, second-harmonic generation; *Q*, quality factor; BIC, bound-state-in-the-continuum; ISTs, intersubband transitions; multi-QW, multiquantum-wells; MD, magnetic dipole; FTIR, Fourier-transform infrared spectroscopy; NA, numerical aperture; MQ, magnetic quadrupole

■ REFERENCES

(1) Boyd, R. W. *Nonlinear Optics*; Academic Press: New York, 2008.
(2) Krasnok, A.; Tymchenko, M.; Alu, A. Nonlinear Metasurfaces: A Paradigm Shift in Nonlinear Optics. *Mater. Today* **2018**, *21* (1), 8−21.
(3) Brener, I.; Liu, S.; Staude, I.; Valentine, J.; Holloway, C. *Dielectric Metamaterials: Fundamentals, Designs and Applications*; Woodhead Publishing, 2019.
(4) Kivshar, Y. All-Dielectric Meta-Optics and Non-Linear Nanophotonics. *National Science Rev.* **2018**, *5* (2), 144−158.
(5) Liu, S.; Sinclair, M. B.; Saravi, S.; Keeler, G. A.; Yang, Y.; Reno, J.; Peake, G. M.; Setzpfandt, F.; Staude, I.; Pertsch, T.; Brener, I. Resonantly Enhanced Second-Harmonic Generation Using III-V Semiconductor All-Dielectric Metasurfaces. *Nano Lett.* **2016**, *16* (9), 5426−5432.
(6) Liu, S.; Keeler, G. A.; Reno, J. L.; Sinclair, M. B.; Brener, I. III-V Semiconductor Nanoresonators − A New Strategy for Passive, Active, and Nonlinear All-Dielectric Metamaterials. *Advanced Opt. Materials* **2016**, *4* (10), 1457−1462.
(7) Liu, S.; Vabishchevich, P. P.; Vaskin, A.; Reno, J. L.; Keeler, G. A.; Sinclair, M. B.; Staude, I.; Brener, I. An All-Dielectric Metasurface as a Broadband Optical Frequency Mixer. *Nature Commun.* **2018**, *9*, 2507.
(8) Camacho-Morales, R.; Rahmani, M.; Kruk, S.; Wang, L.; Xu, L.; Smirnova, D. A.; Solntsev, A. S.; Miroshnichenko, A.; Tan, H. H.; Karouta, F.; Naureen, S.; Vora, K.; Carletti, L.; De Angelis, C.; Jagadish, C.; Kivshar, Y. S.; Neshev, D. N. Nonlinear Generation of Vector Beams from AlGaAs Nanoantennas. *Nano Lett.* **2016**, *16* (11), 7191−7197.
(9) Melik-Gaykazyan, E. V.; Koshelev, K. L.; Choi, J. H.; Kruk, S. S.; Park, H. G.; Fedyanin, A. A.; Kivshar, Y. S. Enhanced Second-Harmonic Generation with Structured Light in AlGaAs Nanoparticles Governed by Magnetic Response. *JETP Lett.* **2019**, *109*, 131−135.
(10) Wolf, O.; Campione, S.; Benz, A.; Ravikumar, A. P.; Liu, S.; Luk, T. S.; Kadlec, E. A.; Shaner, E. A.; Klem, J. F.; Sinclair, M. B.; Brener, I. Phased-Array Sources Based on Nonlinear Metamaterial Nanocavities. *Nature Communication* **2015**, *6*, 7667.
(11) Tymchenko, M.; Gomez-Diaz, J. S.; Lee, J.; Nookala, N.; Belkin, M. A.; Alu, A. Gradient Nonlinear Pancharatnam-Berry Metasurfaces. *Phys. Rev. Lett.* **2015**, *115*, 207403.
(12) Nookala, N.; Lee, J.; Tymchenko, M.; Gomez-Diaz, J. S.; Demmerle, F.; Boehm, G.; Lai, K.; Shvets, G.; Amann, M.-C.; Alu, A.; Belkin, M. Ultrathin Gradient Nonlinear Metasurface with a Giant Nonlinear Response. *Optica* **2016**, *3*, 283−288.
(13) Wang, L.; Kruk, S.; Koshelev, K.; Kravchenko, I.; Luther-Davies, B.; Kivshar, Y. Nonlinear Wavefront Control with All-Dielectric Metasurfaces. *Nano Lett.* **2018**, *18* (6), 3978−3984.
(14) Vabishchevich, P. P.; Liu, S.; Sinclair, M. B.; Keeler, G. A.; Peake, G. M.; Brener, I. Enhanced Second-Harmonic Generation Using Broken Symmetry III-V Semiconductor Fano Metasurfaces. *ACS Photonics* **2018**, *5* (5), 1685−1690.
(15) Liu, Z.; Xu, Y.; Lin, Y.; Xiang, J.; Feng, T.; Cao, Q.; Li, J.; Lan, S.; Liu, J. High-Q Quasibound States in the Continuum for Nonlinear Metasurfaces. *Phys. Rev. Lett.* **2019**, *123*, 253901.
(16) Koshelev, K.; Kruk, S.; Gaykazyan, E. M.; Choi, J. H.; Bogdanov, A.; Park, H. G.; Kivshar, Y. Subwavelength Dielectric Resonators for Nonlinear Nanophotonics. *Science* **2020**, *367* (6475), 288−292.
(17) Anthur, A. P.; Zhang, H.; Paniagua-Dominguez, R.; Kalashnikov, D. A.; Ha, S. T.; Maß, T. W. W.; Kuznetsov, A. I.; Krivitsky, L. Continuous Wave Second Harmonic Generation Enabled by Quasi-Bound-States in the Continuum on Gallium Phosphide Metasurfaces. *Nano Lett.* **2020**, *20* (12), 8745−8751.
(18) Marino, G.; Rocco, D.; Gigli, C.; Beaudoin, G.; Pantzas, K.; Suffit, S.; Filloux, P.; Sagnes, I.; Leo, G.; De Angelis, C. Harmonic Generation with Multi-Layer Dielectric Metasurfaces. *Nanophotonics* **2021**, *10* (7), 1837−1843.
(19) Carletti, L.; Locatelli, A.; Stepanenko, O.; Leo, G.; De Angelis, C. Enhanced Second-Harmonic Generation from Magnetic Resonance in AlGaAs Nanoantennas. *Optics Exp.* **2015**, *23* (20), 26544−26550.
(20) Frizyuk, K. Second-harmonic generation in dielectric nanoparticles with different symmetries. *JOSA B* **2019**, *36* (8), F32−F37.
(21) Rocco, D.; Gigli, C.; Carletti, L.; Marino, G.; Vincenti, M. A.; Leo, G.; Angelis, C. D. Vertical Second Harmonic Generation in Asymmetric Dielectric Nanoantennas. *IEEE Photonics Journal* **2020**, *12* (3), 1−7.
(22) Xu, L.; Rahmani, M.; Smirnova, D.; Kamali, K. Z.; Zhang, G.; Neshev, D.; Miroshnichenko, A. E. Highly-Efficient Longitudinal Second-Harmonic Generation from Doubly-Resonant AlGaAs Nanoantennas. *Photonics* **2018**, *5* (3), 29.
(23) Lochner, F. J. F.; Fedotova, A. N.; Liu, S.; Keeler, G. A.; Peake, G. M.; Saravi, S.; Shcherbakov, M. R.; Burger, S.; Fedyanin, A. A.; Brener, I.; Pertsch, T.; Setzpfandt, F.; Staude, I. Polarization-Dependent Second Harmonic Diffraction from Resonant GaAs Metasurfaces. *ACS Photonics* **2018**, *5* (5), 1786−1793.
(24) Carletti, L.; Locatelli, A.; Neshev, D.; De Angelis, C. Shaping the Radiation Pattern of Second-Harmonic Generation from AlGaAs Dielectric Nanoantennas. *ACS Photonics* **2016**, *3* (8), 1500−1507.
(25) Sautter, J. D.; Xu, L.; Miroshnichenko, A. E.; Lysevych, M.; Volkovskaya, I.; Smirnova, D. A.; Camacho-Morales, R.; Zangeneh Kamali, K.; Karouta, F.; Vora, K.; Tan, H. H.; Kauranen, M.; Staude, I.; Jagadish, C.; Neshev, D. N.; Rahmani, M. Tailoring Second-Harmonic Emission from (111)-GaAs Nanoantennas. *Nano Lett.* **2019**, *19*, 3905−3911.

https://doi.org/10.1021/acs.nanolett.1c03325
Nano Lett. 2022, 22, 896−903

(26) Xu, L.; Saerens, G.; Timofeeva, M.; Smirnova, D. A.; Volkovskaya, I.; Lysevych, M.; Camacho-Morales, R.; Cai, M.; Kamali, K. Z.; Huang, L.; Karouta, F.; Tan, H. H.; Jagadish, C.; Miroshnichenko, A. E.; Grange, R.; Neshev, D. N.; Rahmani, M. Forward and Backward Switching of Nonlinear Unidirectional Emission from GaAs Nanoantennas. *ACS Nano* **2020**, *14* (2), 1379−1389.
(27) Tsia, K. K.; Fathpour, S.; Jalali, B. Energy Harvesting in Silicon Wavelength Converters. *Optics Exp.* **2006**, *14* (25), 12327−12333.
(28) Capasso, F.; Sirtori, C.; Cho, A. Coupled Quantum Well Semiconductors with Giant Electric Field Tunable Nonlinear Optical Properties in the Infrared. *IEEE J. Quantum Electron.* **1994**, *30*, 1313−1326.
(29) Lee, J.; Tymchenko, M.; Argyropoulos, C.; Chen, P.; Lu, F.; Demmerle, F.; Boehm, G.; Amann, M. C.; Alu, A.; Belkin, M. A. Giant Nonlinear Response from Plasmonic Metasurfaces Coupled to Intersubband Transitions. *Nature* **2014**, *511*, 65.
(30) Lee, J.; Nookala, N.; Gomez-Diaz, J. S.; Tymchenko, M.; Demmerle, F.; Boehm, G.; Amann, M. C.; Alu, A.; Belkin, M. A. Ultrathin Second-Harmonic Metasurfaces with Record-High Nonlinear Optical Response. *Adv. Optical Mater.* **2016**, *4* (5), 664−670.
(31) Sarma, R.; de Ceglia, D.; Nookala, N.; Vincenti, M. A.; Campione, S.; Wolf, O.; Scalora, M.; Sinclair, M. B.; Belkin, M. A.; Brener, I. Broadband and Efficient Second-Harmonic Generation from a Hybrid Dielectric Metasurface/Semiconductor Quantum-Well Structure. *ACS Photonics* **2019**, *6* (6), 1458−1465.
(32) Sarma, R.; Xu, J.; de Ceglia, D.; Klem, J.; Sinclair, M.; Belkin, M. A.; Brener, I. Control of Second-Harmonic Generation in Dielectric Polaritonic Metasurfaces Using $\chi^{(2)}$ Polarity Switching. *Conference on Lasers and Electro-Optics*; OSA Technical Digest, 2021; paper FM3I.2, San Jose, California United States, 9−14 May 2021.
(33) Dini, D.; Kohler, R.; Tredicucci, A.; Biasiol, G.; Sorba, L. Microcavity Polariton Splitting of Intersubband Transitions. *Phys. Rev. Lett.* **2003**, *90* (11), 116401.
(34) Wolf, O.; Allerman, A. A.; Ma, X.; Wendt, J. R.; Song, A. Y.; Shaner, E. A.; Brener, I. Enhanced Optical Nonlinearities in the Near-Infrared Using III-Nitride Heterostructures Coupled to Metamaterials. *Appl. Phys. Lett.* **2015**, *107*, 151108.
(35) Nevou, L.; Tchernycheva, M.; Julien, F.; Raybaut, M.; Godard, A.; Rosencher, E.; Guillot, F.; Monroy, E. Intersubband Resonant Enhancement of Second-Harmonic Generation in GaN/AlN Quantum Wells. *Appl. Phys. Lett.* **2006**, *89*, 151101.
(36) Laffaille, P.; Manceau, J. M.; Laurent, T.; Bousseksou, A.; Le Gratiet, L.; Teissier, R.; Baranov, A. N.; Colombelli, R. Intersubband Polaritons at $\lambda \sim 2$ μm in the InAs/AlSb system. *Appl. Phys. Lett.* **2018**, *112*, 201113.
(37) Rosencher, E.; Fiore, A.; Vinter, B.; Berger, V.; Bois, Ph.; Nagle, J. Quantum Engineering of Optical Nonlinearities. *Science* **1996**, *271*, 168−173.
(38) Rosencher, E. Towards Integrated Semiconductor Optical Parametric Oscillators. *Comptes Rendus de l'Académie des Sciences-Series IV-Physics* **2000**, *1* (5), 615−625.
(39) Santiago-Cruz, T.; Fedotova, A.; Sultanov, V.; Weissflog, M. A.; Arslan, D.; Younesi, M.; Pertsch, T.; Staude, I.; Setzpfandt, F.; Chekhova, M. Photon Pairs from Resonant Metasurfaces. *Nano Lett.* **2021**, *21*, 4423−4429.
(40) Tokman, M.; Long, Z.; AlMutairi, S.; Wang, Y.; Vdovin, V.; Belkin, M.; Belyanin, A. Purcell Enhancement of the Parametric Down-Conversion in Two-Dimensional Nonlinear Materials. *APL. Photonics* **2019**, *4*, 034403.
(41) Jung, D.; Bank, S.; Lee, M. L.; Wasserman, D. Next-Generation Mid-Infrared Sources. *Journal of Optics* **2017**, *19* (12), 123001.
(42) Haas, J.; Mizaikoff, B. Advances in Mid-Infrared Spectroscopy for Chemical Analysis. *Annual Review of Analytical Chemistry* **2016**, *9*, 45−68.
(43) Qu, Z.; Jiang, P.; Zhang, W. Development and Application of Infrared Thermography Non-Destructive Testing Techniques. *Sensors* **2020**, *20* (14), 3851.
(44) Hermes, M; Morrish, R B.; Huot, L; Meng, L; Junaid, S; Tomko, J; Lloyd, G R; Masselink, W T; Tidemand-Lichtenberg, P; Pedersen, C; Palombo, F; Stone, N Mid-IR Hyperspectral Imaging for Label-Free Histopathology and Cytology. *Journal of Optics* **2018**, *20* (2), 023002.
(45) Colley, C. S.; Hebden, J. C.; Delpy, D. T.; Cambrey, A. D.; Brown, R. A.; Zibik, E. A.; Ng, W. H.; Wilson, L. R.; Cockburn, J. W. Mid-Infrared Optical Coherence Tomography. *Rev. Sci. Instrum.* **2007**, *78* (12), 123108.

https://doi.org/10.1021/acs.nanolett.1c03325
Nano Lett. 2022, 22, 896−903